e-Prime - Advances in Electrical Engineering, Electronics and Energy 12 (2025) 101028

Contents lists available at ScienceDirect

e-Prime - Advances in Electrical Engineering, Electronics and Energy

journal homepage: www.elsevier.com/locate/prime

Analysis of the ZVS operating range of input-series output-series DC–DC DAB converters for MV DC microgrids using different modulators to control the power flow

D. Garrido [a,b,*], F. Rodríguez [a,b], J. Bosso [b,c], G. Oggier [a,b]

[a] Grupo de Electrónica Aplicada (GEA), Instituto de Investigaciones en Tecnologías Energéticas y Materiales Avanzados (IITEMA), Universidad Nacional de Río Cuarto (UNRC), Ruta #36, km. 601, Río Cuarto, 5800, Córdoba, Argentina

[b] Consejo Nacional de Investigaciones Científicas y Técnicas (CONICET), Argentina

[c] Universidad Nacional de Villa Mercedes (UNViMe), Balcarce 314, Villa Mercedes, 5730, San Luis, Argentina

ARTICLE INFO

Keywords:
DAB converter
ISOS connection
Soft-switching
ZVS
Medium voltage DC microgrids

ABSTRACT

This paper analyzes the input-series-output-series (ISOS) connection of dual active bridge (DAB) modules for medium voltage DC microgrids using different modulators: first using a unique modulator that allows controlling of the power flow of all modules, which is a more straightforward solution, and then using independent modulators to facilitate the voltage balance and the power transference of each one. In this analysis, parametric differences between the modules are considered, and the voltage distribution between the modules, the ZVS conditions, and the transferred power as a function of the main converter parameters design are obtained. Finally, experimental results of a scaled-down 500 W prototype demonstrate the proposal's feasibility.

1. Introduction

The integration of renewable energy sources in medium-voltage (MV) microgrids requires power electronic converters to control the power transfer and to adapt variable voltage levels, as well as to enable the interconnection of both DC and AC sources and loads. In these applications, appropriate topologies and modulation techniques are required to reduce semiconductor devices' electrical stresses (overvoltage and overcurrent) [1].

One possibility is the series connection of semiconductor devices, which allows conventional topologies but requires a proper equalization of dynamic and static voltage distribution between the devices [2]. Another possibility is to use multilevel converters, but in topologies with more than three levels, the complexity of construction and its modulation and control strategies increases [3]. A third option is to use series-connected modules, whose modulation and control strategies can be simpler than those used in multilevel topologies [3–5]. The main advantages of a modular converter include ease of thermal sizing since each module handles a portion of the total processed power and increased overall system reliability due to reduced thermal and electrical stress on semiconductors and passive components. Furthermore, modular converters allow faster, more straightforward, and lower-cost design procedures for the entire system compared to multilevel options, such as modularity, which makes it easier to increase system capacity by adding modules in series and parallel.

This paper analyzes a modular converter for MV DC microgrid applications implemented with modules in input-series-output-series (ISOS) connection [5]. A challenge in the design of these systems is to achieve adequate voltage sharing at the series ports of the modules since the parametric differences between the magnetic components and the semiconductor devices due to the manufacturing process, aging, or operating conditions can produce imbalances in the DC voltages of the modules [6,7]. These voltage imbalances cause an unequal power distribution that can accelerate the ages of the modules that transfer the most power or lead to the hard-switching operation of one or more modules, reducing overall system efficiency. Besides the differences in voltage levels, the power transferred by each module differs proportionally to the parametric variations, and consequently, some modules can overheat and be prone to failure.

In the bibliography, some studies analyze strategies to balance the voltages of each module. For applications with unidirectional energy flow, the connection of full-bridge, forward, and flyback modules has been studied, among others [8–10]. When bidirectional flow is required, it is possible to use half-bridge single-phase topologies, DC–DC

* Corresponding author at: Grupo de Electrónica Aplicada (GEA), Instituto de Investigaciones en Tecnologías Energéticas y Materiales Avanzados (IITEMA), Universidad Nacional de Río Cuarto (UNRC), Ruta #36, km. 601, Río Cuarto, 5800, Córdoba, Argentina.
E-mail address: daniel.oscar.garrido@ing.unrc.edu.ar (D. Garrido).

https://doi.org/10.1016/j.prime.2025.101028
Received 30 December 2024; Received in revised form 13 May 2025; Accepted 20 May 2025
Available online 30 May 2025

converters with dual active bridges (DAB), and resonant series, among others [11,12]. The DAB converter is a topology widely used in MV microgrids, electric and hybrid vehicles, and solid-state transformers (SST) due to its outstanding electrical characteristics, such as galvanic isolation, zero-voltage switching (ZVS) operation, simple power flow control, and the possibility to reduce or increase the voltage [13,14]. An analysis demonstrating the stable operation of the ISOS modular connection of DAB converters when using a unique modulator was presented in [15].

This paper presents an analysis of the ISOS connection of DAB converter modules used in MV DC microgrid applications, considering two methods to control the power transfer. The first strategy involves using a unique modulator to control all the modules of the converter, simplifying its power setup and operation. However, one of the features of using this strategy is that the DC port voltages cannot be balanced in the presence of parametric differences between the DAB modules. The second method uses independent modulators, which increases the complexity but allows for the balancing of the DC port voltages and power transfer of each module. This analysis enables the voltage distribution to be established and their power transferred as a function of the DAB module parameters. The study established conditions for determining the best strategy for each application in terms of implementation complexity, overall system efficiency, power transfer capability, and control capacity to balance voltages and power transfer. In contrast to previous research, this paper also analyzes the ZVS conditions of the modular converter to establish the operating range with low switching losses as a function of the parameters of each DAB module, which allows for reducing sudden voltage and current variations, stress, and losses on semiconductor devices. Experimental results obtained with a laboratory prototype are presented to demonstrate the practical feasibility of the proposal.

This article is organized as follows: Section 2 describes the topology, modeling, and ZVS conditions' DAB converter. Section 3 presents the steady-state model of n DAB modules connected in series at the input and the output. Section 4 includes experimental results to validate the presented analysis. Finally, the conclusions are given in Section 5.

2. DAB x converter description

In this Section, the main operating characteristics of the DAB x converter are summarized to facilitate the analysis of the modular converter presented in the following sections, where the notation $x = 1, 2, \ldots, n$ is used to indicate the DAB module number. The steady-state model of the DAB converter has been deduced in several papers in the literature, so the articles [16–18], among others, can be consulted for a more detailed description.

Fig. 1 shows the topology of the DAB x converter. This article considers the single phase shift (SPS) modulation strategy, which generates two square AC voltage waveforms v_{Tx1} and v_{Tx2}, with a duty cycle of 50% and constant frequency. The power transfer is controlled by applying a specific phase shift Δ_x between the voltages v_{Tx1} and v_{Tx2}, applied to terminals of the transformer T_x [16]. Each semiconductor device, S_{xz}, shown in Fig. 1, is implemented with a transistor T_{xz}, a diode D_{xz} and a capacitor C_{xz}, where $z = 1, 2, \ldots, 8$ indicates the semiconductor device number belonging to the DAB module x. The transformer is modeled by its leakage inductance, L_x. Thus, the converter can be represented by two active bridges B_{x1} and B_{x2}, connected by L_x and an ideal transformer T_x. To simplify the analysis, the transformer ratio, r, is considered equal to 1.

Fig. 2 shows the waveforms of the voltages v_{Tx1} and v_{Tx2}, the current i_{Lx} of the transformer, and the currents i_{Bx1} and i_{Bx2} of the active bridges B_{x1} and B_{x2}, respectively. This figure corresponds to a power transfer from v_{x1} to v_{x2}, notations V_{x1} and V_{x2} represent the DC components of the voltages v_{x1} and v_{x2}, respectively. From these waveforms in the figure, it can be demonstrated that the first two intervals of each switching cycle, determined by the phase shift Δ_x, are sufficient to evaluate the evolution of the converter DC port voltages and currents.

The current i_{Lx} of the leakage inductance L_x can be expressed as a function of the angle $\theta = \omega t$, where $\omega = 2\pi f_s$ is the angular frequency, f_s is the switching frequency, and t is the time. These relations for each interval can be expressed as follows: For $0 \le \theta \le \Delta_x$,

$$i_{Lx}(\theta) = \left(\frac{V_{x1} + V_{x2}}{\omega L_x}\right)\theta + i_{Lx}(0). \tag{1}$$

For $\Delta_x \le \theta \le \pi$,

$$i_{Lx}(\theta) = \left(\frac{V_{x1} - V_{x2}}{\omega L_x}\right)(\theta - \Delta_x) + i_{Lx}(\Delta_x). \tag{2}$$

The average value of the current i_{Lx} must be zero in steady-state in a switching period to avoid saturation of the transformer core, so it must be fulfilled that $i_{Lx}(0) = -i_{Lx}(\pi)$. Considering this condition and Eqs. (1) and (2), it can be obtained,

$$i_{Lx}(0) = -\left(\frac{V_{x1}(2d_x\Delta_x + \pi - d_x\pi)}{2\omega L_x}\right), \tag{3}$$

where $d_x = V_{x2}/V_{x1}$, is the voltage conversion ratio of the DAB x module.

Based on the Eqs. (1) to (3), the average power transferred by the converter can be calculated through the following expression,

$$P_x = \frac{1}{\pi}\int_0^{\pi} v_{Tx1}(\theta) i_{Lx}(\theta) d\theta = \frac{V_{x1}^2 d_x \Delta_x (\pi - |\Delta_x|)}{\omega L_x \pi}. \tag{4}$$

In this manner, the phase shift Δ_x controls the power flow of the converter.

For the circuit in Fig. 1, in steady state, it is satisfied that $I_{Bx2} = I_2$ and $I_{Bx1} = I_1$, where notations I_{Bx1}, I_{Bx2}, I_1, and I_2 represent the DC components of the currents i_{Bx1}, i_{Bx2}, i_1, and i_2, respectively. Therefore the average currents of the DAB converter can be expressed as,

$$\begin{aligned} I_{Bx1} &= \frac{1}{\pi}\left(\int_0^{\Delta_x} i_{Lx}(\theta)d\theta + \int_{\Delta_x}^{\pi} i_{Lx}(\theta)d\theta\right) = \frac{(\pi - |\Delta_x|)\,\Delta_x V_{x2}}{\omega L_x \pi}, \\ I_{Bx2} &= \frac{1}{\pi}\left(\int_0^{\Delta_x} -i_{Lx}(\theta)d\theta + \int_{\Delta_x}^{\pi} i_{Lx}(\theta)d\theta\right) = \frac{(\pi - |\Delta_x|)\,\Delta_x V_{x1}}{\omega L_x \pi}. \end{aligned} \tag{5}$$

2.1. ZVS conditions

In order to achieve ZVS turn-on operation, when the turn-on signal is applied, the initial direction of the current flow must ensure that antiparallel diodes D_{xz} of the DAB modules start conducting before its corresponding transistor T_{xz}, causing the voltage across the device to be zero. In this manner, the transistor T_{xz} naturally starts conducting when the direction of current flow is reversed, resulting in zero turn-on losses [19]. On the other hand, to achieve ZVS turn-off operation in all semiconductor devices, when T_{xz} receives the turn-off signal, they should be conducting. As a consequence, the current should be transferred from the transistor to the capacitor connected in parallel, C_{xz}. Usually, this capacitor is the device's output capacitance. As a consequence, this condition allows a reduced voltage across the switch during its turn-off interval, reducing the switching losses [17]. This operation is defined as ZVS soft-switching operation mode [19]. Therefore, to obtain ZVS in the devices of the active bridge B_{x1}, it must be satisfied that $i_{Lx}(\pi) \ge 0$, and in the active bridge B_{x2}, it must be satisfied that $i_{Lx}(\Delta_x) \ge 0$ [16]. Considering the above, the ZVS operation region obtained for the active bridge B_{x2} is described by the following condition,

$$\Delta_x \ge \frac{(1 - d_x)\pi}{2}, \tag{6}$$

in buck mode ($d_x < 1$). Likewise, the ZVS condition for the active bridge B_{x1} results,

$$\Delta_x \ge \frac{(d_x - 1)\pi}{2d_x}, \tag{7}$$

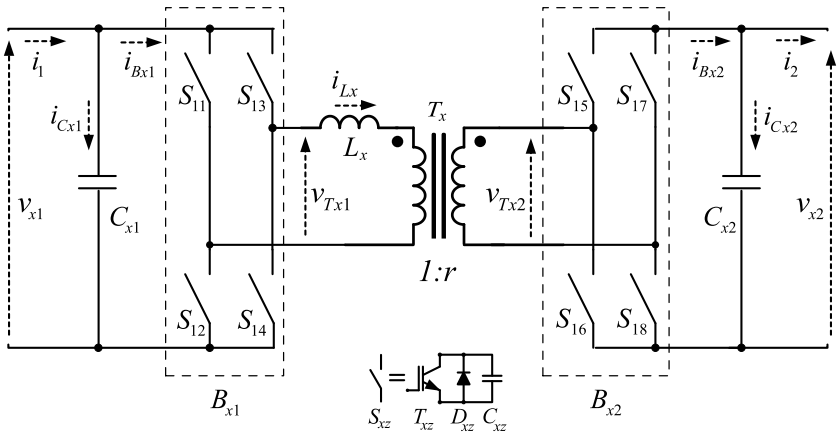

Fig. 1. Simplified diagram of the DAB converter.

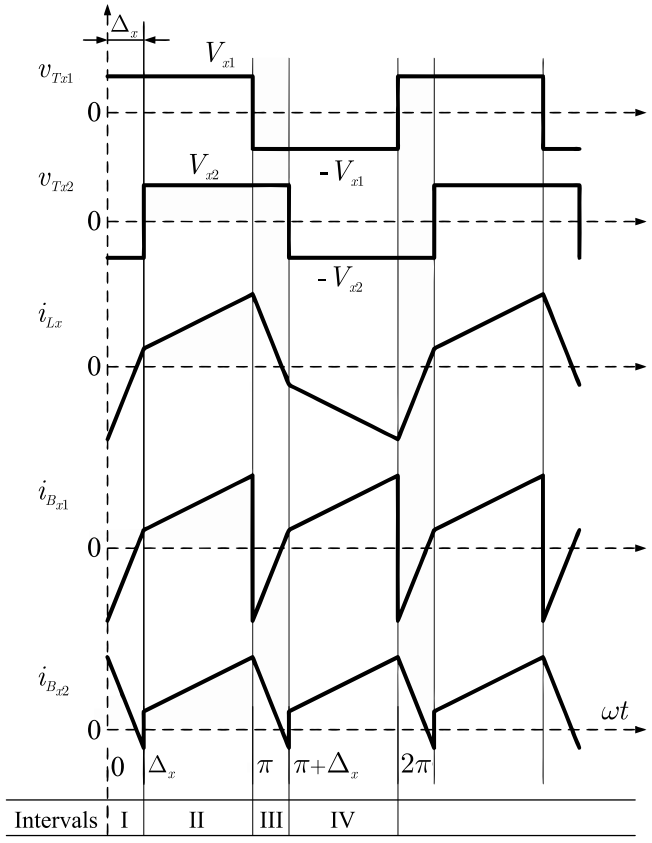

Fig. 2. Waveforms of the voltages, v_{Tx1} and v_{Tx2}, and of the currents i_{Lx}, i_{Bx1} and i_{Bx2}, for $v_{x1} > v_{x2}$ with power transfer from v_{x1} to v_{x2}.

in boost mode ($d_x > 1$). With these conditions established, the ZVS region is obtained, which can be represented in a nomogram like the one proposed [17]. In such a nomogram, the voltage conversion ratio, d_x, is plotted as a function of the normalized output current of each DAB x module, $I_{Bx2}(pu)$, being its base current,

$$I_{base_x} = \frac{V_{x1}}{\omega L_x}. \tag{8}$$

3. Analysis of n DAB modules in ISOS connection

From the x DAB converter model developed in the previous Section, it is possible to extend the steady-state model to n DAB modules in an ISOS connection, as shown in Fig. 3. The system expressions are presented as a function of the modular converter parameters and the phase shift Δ_x applied to each module, considering differences in the values of the leakage inductances L_x of each DAB module.

For the circuit of Fig. 3 with n DAB modules in ISOS connection in steady-state, it is satisfied,

$$I_1 = I_{Bx1}, \quad I_2 = I_{Bx2}, \tag{9}$$

$$\sum_{x=1}^{n} V_{x1} = V_1, \quad \sum_{x=1}^{n} V_{x2} = V_2, \tag{10}$$

where notations V_1 and V_2 represent the DC components of the voltages v_1 and v_2, respectively.

Given the Eqs. (1) and (2) of the current in the transformer and the procedure developed in Section 2, the average currents of the DAB x module of the circuit in Fig. 3 can be obtained as,

$$I_{Bx1} = a_x V_{x2}, \quad I_{Bx2} = a_x V_{x1}, \tag{11}$$

where,

$$a_x = \frac{(\pi - |\Delta_x|)\Delta_x}{\omega L_x \pi}. \tag{12}$$

In the modular converter of Fig. 3, it is satisfied that $I_1 = (V_{DC} - V_1)/R_S$ and $I_2 = V_2/R_L$, where R_S represents the series resistance of the voltage source V_{DC}, and R_L represents the resistive load. Hence, from Eqs. (9) to (12), it is possible to express the voltages V_1 and V_2 as follows,

$$V_1 = \frac{V_{DC}}{\left[1 + \frac{R_S R_L}{n^2}\left(\frac{a_1 L_1}{n L_a} + \frac{a_2 L_2}{n L_a} + \ldots + \frac{a_n L_n}{n L_a}\right)^2\right]}, \tag{13}$$

$$V_2 = \frac{R_L}{n} V_1 \left(\frac{a_1 L_1}{n L_a} + \frac{a_2 L_2}{n L_a} + \cdots + \frac{a_n L_n}{n L_a}\right), \tag{14}$$

where,

$$L_a = \frac{L_1 + L_2 + \cdots + L_n}{n}, \tag{15}$$

is defined as the average leakage inductance of the modular converter. From the developed model and the ZVS conditions obtained for the DAB x module using the SPS modulation strategy, it is possible to propose two methods to control the power transferred by the modular converter. These two methods consist of using a unique modulator for all the DAB modules to obtain simplicity in the power transfer control or using independent modulators to balance the power transferred by each module. Therefore, in the following sections for both methods, the DC ports' voltage distribution, the power transferred by each DAB module, and the ZVS operating region of the modular converter are analyzed.

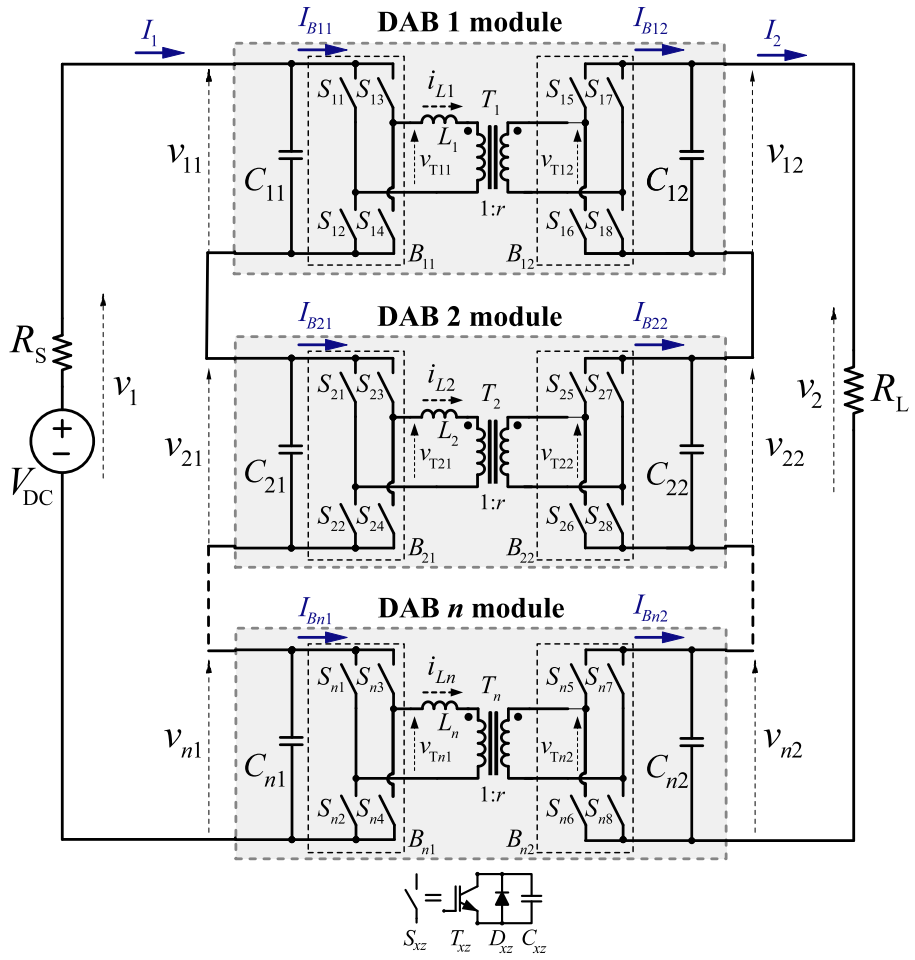

Fig. 3. ISOS connection of n DAB modules.

3.1. Analysis using a unique modulator

When a unique modulator is used, the same phase shift is applied at the n DAB modules to control the power flow, so it is satisfied that $\Delta_1 = \Delta_2 = \cdots = \Delta_n = \Delta$. By using this method of power transfer control, the average currents of the DAB x module of the circuit in Fig. 3 can be expressed as,

$$I_{Bx1} = \frac{(\pi - |\Delta|)\Delta V_{x2}}{\omega L_x \pi}, \quad I_{Bx2} = \frac{(\pi - |\Delta|)\Delta V_{x1}}{\omega L_x \pi}. \tag{16}$$

From Eqs. (9), (10) and (16), the following expressions can be obtained,

$$\frac{V_1}{nL_a} = \frac{V_{x1}}{L_x}, \quad \frac{V_2}{nL_a} = \frac{V_{x2}}{L_x}. \tag{17}$$

The voltage conversion ratio of each module can be determined by dividing the two expressions of Eq. (17). It is obtained that: $d = V_2/V_1 = V_{12}/V_{11} = V_{22}/V_{21} = \cdots = V_{n2}/V_{n1}$. Therefore, the n DAB modules in ISOS connection operate with the same voltage conversion ratio as the modular converter. In addition, the V_{xy} voltages of the DC ports of each DAB module can be obtained as a function of the leakage inductances as,

$$V_{xy} = V_y \left(\frac{L_x}{L_1 + L_2 + \cdots + L_n} \right) = V_y \left(\frac{L_x}{nL_a} \right), \tag{18}$$

where $y = 1$ or 2 indicates whether the variable belongs to the input or output port, respectively. In this expression, it can be seen that the voltages V_{xy} are a function of the ratio between the leakage inductance of each module concerning n times the average leakage inductance value of the modular converter.

From the Eqs. (16) and (17), the average input and output currents can be expressed as,

$$I_1 = \frac{V_2 (\pi - |\Delta|) \Delta}{\omega n L_a \pi}, \quad I_2 = \frac{V_1 (\pi - |\Delta|) \Delta}{\omega n L_a \pi}. \tag{19}$$

Therefore, the transferred power is obtained as,

$$P_o = V_2 I_2 = \frac{V_1 V_2 \Delta (\pi - |\Delta|)}{\omega n L_a \pi}. \tag{20}$$

From the above equations, it is possible to express the output power of the modular converter as the sum of the powers transferred by each of the DAB modules,

$$P_o = P_1 + P_2 + \cdots + P_n = \sum_{x=1}^{n} \frac{V_{x1} V_{x2} (\pi - |\Delta|) \Delta}{\omega L_x \pi}, \tag{21}$$

where the power transferred by each module is obtained by replacing Eq. (18) in (21), resulting in,

$$P_o = P_1 + P_2 + \cdots + P_n = \\ = L_1 \frac{V_1 V_2 (\pi - |\Delta|) \Delta}{(nL_a)^2 \omega \pi} + L_2 \frac{V_1 V_2 (\pi - |\Delta|) \Delta}{(nL_a)^2 \omega \pi} + \cdots + L_n \frac{V_1 V_2 (\pi - |\Delta|) \Delta}{(nL_a)^2 \omega \pi}. \tag{22}$$

Last expression shows that each module transfers a power proportional to its leakage inductance when a unique modulator is used.

3.2. Analysis using independent modulators

This subsection presents an analysis to achieve a balanced distribution of the V_{xy} voltages of the DC ports of the modules. From Eqs. (9),

(11) and (12), it is concluded that this condition can be achieved by applying a specific phase shift Δ_x to each module such that the following relationship is fulfilled,

$$a_1 = a_2 = \cdots = a_n = a. \tag{23}$$

Replacing Eq. (12) in (23), yields,

$$\frac{\Delta_1\left(\pi - |\Delta_1|\right)}{\omega L_1 \pi} = \frac{\Delta_2\left(\pi - |\Delta_2|\right)}{\omega L_2 \pi} = \cdots = \frac{\Delta_n\left(\pi - |\Delta_n|\right)}{\omega L_n \pi}, \tag{24}$$

where it can be deduced that it is possible to balance the voltages V_{xy} under parametric differences, by applying the correct phase shift to each module, obtaining,

$$\begin{aligned} V_{11} = V_{21} = \cdots = V_{n1} = V_1/n \\ V_{12} = V_{22} = \cdots = V_{n2} = V_2/n \end{aligned} \tag{25}$$

Because the voltages are balanced, the n DAB modules are determined to have the same voltage conversion ratio as the modular converter: $d = V_2/V_1 = V_{12}/V_{11} = V_{22}/V_{21} = \cdots = V_{n2}/V_{n1}$.

The power transferred by the modular converter can be expressed by solving the Eqs. (9) and (25), yielding,

$$P_o = V_{12}V_{11}a_1 + V_{22}V_{21}a_2 + \ldots + V_{n2}V_{n1}a_n = \frac{V_2 V_1 a}{n}. \tag{26}$$

Under the assumption that the voltages V_{xy} are balanced when the idealized condition $a_1 = a_2 = \cdots = a_n = a$ is satisfied; consequently, all modules transfer the same power when the modules present parametric variations. However, in an experimental setup, the tolerances associated with the values of L_x can produce slight imbalances in the powers transferred by the modules when the phase shifts Δ_x established according to (23) are applied.

3.3. Soft-switching conditions

The conditions presented in Section 2.1 are applied for each n DAB module, and the ZVS region represented in a nomogram can be obtained. In this nomogram, the voltage conversion ratio, d_x, is plotted as a function of the normalized output current of each DAB module, $I_{Bx2}(pu)$, with its base current, $I_{base_x} = V_{x1}/(\omega L_x)$. Furthermore, it defines the normalized load for the modular converter as $R = R_L/(\omega\, nL_a)$.

In Section 4, the nomogram corresponding to the implemented modular converter is presented, where the ZVS region obtained from the active bridge B_{x1} is described by the condition, $\Delta_x > ((1 - d_x)\pi/2)$ for $d_x < 1$, and from the active bridge B_{x2} it obtains the condition, $\Delta_x > ((d_x - 1)\pi/(2d_x))$ for $d_x > 1$.

4. Experimental results

This Section presents experimental results with three DAB modules in ISOS connection for the two power transfer control methods presented in Sections 3.1 and 3.2, which allow the presented analysis to be validated.

Fig. 4 shows the block diagram of the experimental prototype, where it can be seen that an analog stage processes the measurements of the voltages v_{xy} and currents i_{Lx} to determine whether their magnitudes are within the admissible operating range. When a voltage or current variable is greater than the preestablished thresholds, the TripZone protection block is activated, which soft turns off the modular converter to prevent damage. The Single Phase Shift modulator block generates the PWM signals according to the phase shift Δ_x to be applied to each DAB module to control the power transfer. The Gate Drivers block adequate the PWM signals to the voltage levels to ensure the safe turn on and turn off of the semiconductor devices.

A photograph of the implemented prototype, whose parameters are presented in Table 1, is shown in Fig. 5. The active bridges were implemented using discrete MOSFETs, model IPW65R110CFDA 650V-31.2 A.

Table 1
Experimental prototype characteristics.

Parameter	Magnitude	Description
P_o	500 W	maximum output power
V_{DC}	120 V	DC voltage source
R_S	4.5 Ω	series resistance of V_{DC}
R_L	230 Ω	load resistance
R	4.21 [p.u.]	normalized load
n	3	number of modules
f_s	20 kHz	switching frequency
C_{x1}	940 µF	capacitance of input DC ports
C_{x2}	360 µF	capacitance of output DC ports
L_1	140 µH	leakage inductance of T_1
L_2	163.92 µH	leakage inductance of T_2
L_3	130.85 µH	leakage inductance of T_3
r	1	transformation ratio of T_x

Table 2
Parameters of the EE703332 magnetic core.

Parameter	Magnitude	Description
A_L	9500 nH ± 25%	inductance factor
A_c	683 mm^2	effective cross-sectional area
V_e	102400 mm^3	effective magnetic volume
$B_{ac,\text{sat}}$	390 mT	saturation flux density @100 °C
μ_m	2100	material permeability @25 °C

The modulation signals were generated using a TMS320F28377D controller. The magnitudes L_x indicated in Table 1 were established to validate the model against parametric differences. These magnetic components were implemented using ferrite cores and Litz wire windings. Next, a description of the magnetic components and their design considerations are given.

4.1. Magnetic components design considerations

Medium-frequency transformers were implemented for each DAB module to provide galvanic isolation between the input and output ports. As explained before, the power transferred by each DAB module is a function of the leakage inductance of the transformer [16], which requires a precise value of this parameter. Therefore, to achieve a specific power rating for the modular converter, the transformers are designed with minimal leakage inductance. Then, an auxiliary inductor is added in series with the primary winding of the transformer T_x, as shown in Fig. 4, to obtain the desired total leakage inductance L_x [15].

The design of the magnetic components was performed following the general procedure presented in the bibliography [20], considering the parameters of the proposed modular converter and design recommendations from the literature to reduce volume and weight and get low power losses when the voltage and current waveforms are nonsinusoidal [21].

The switching frequency of the converter was chosen to be equal 20 kHz, according to the technology of the semiconductors adopted to get a balance between losses and volume, and Ferrite for the magnetic cores, which is a material with high electrical resistivity and, consequently, low losses associated with eddy currents for the operating frequency. For both the auxiliary inductor and transformer, the E-shape core model EE703332 was utilized for the three DAB modules, whose main parameters are presented in Table 2 [22].

In order to simplify the explanation, Table 3 only presents the main expressions used to design the magnetic components of the modular converter. The number of turns $N_{p,s}$ for the transformers is calculated from Faraday's Law, for a unity turns ratio, where $V_{p,s}$ is the voltage [V] applied to the winding terminals, K_f is the waveform coefficient (usually adopted equal to 4 for a square waveform), B_{ac} is the operating flux density [T], f the operating frequency [Hz], and A_c the effective cross-sectional area [mm^2]. The current density of the transformer windings, J, is expressed in [A/mm^2], which is a function of the

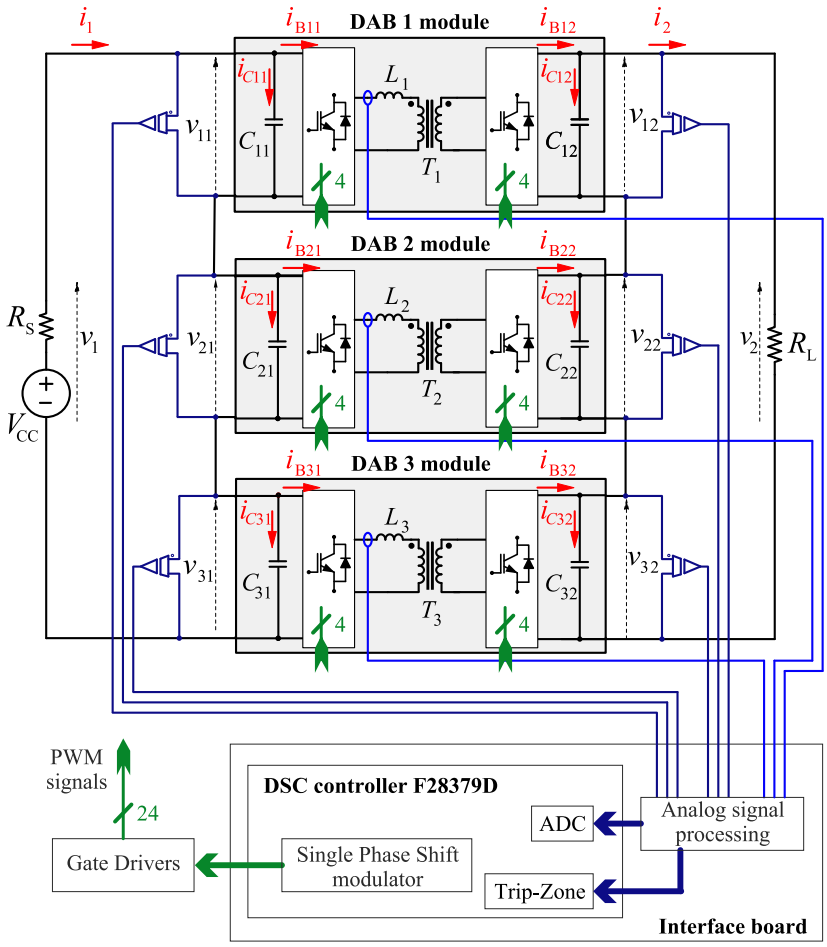

Fig. 4. Block diagram of the experimental prototype.

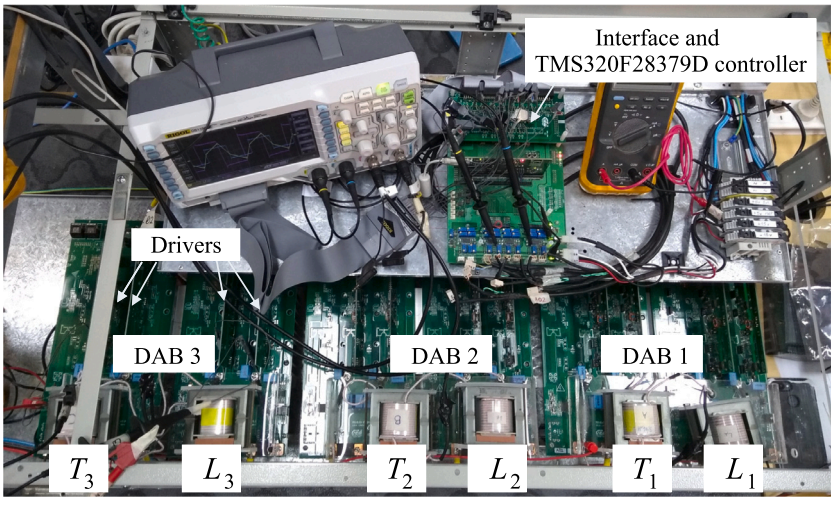

Fig. 5. Photograph of the implemented modular converter.

transformer's apparent power P_t, the window utilization factor K_u, and the area product A_p in [mm^4] given by $A_p = W_a \cdot A_c$, where W_a is the window area.

Regarding the inductors, the number of turns N and the length of the air gap l_g [mm] are established according to the required inductance L [H] and to prevent the saturation of the magnetic core ($B_{ac} \ll B_{ac,\text{sat}}$), by solving the Faraday's Law and Ampere's Law. The resultant inductance is also a function of fringing-flux factor F, which can be estimated as a function of A_c, l_g and the winding length G in [mm].

Table 4 presents all the parameters of the transformers and inductors implemented to obtain the specified leakage inductance L_x in each DAB module to validate the analysis presented in Section 3, considering parametric differences between modules. A photograph of the transformer and auxiliary inductor assembly is shown in Fig. 6. The windings were made with AWG10 Litz wire [23].

Table 3
Equations used in the design of magnetic components.

Transformer	Inductor
$N_{p,s} = \frac{V_{p,s}10^2}{K_f B_{ac} f A_c}$	$N = \frac{V_{ac}10^2}{K_f B_{ac} f A_c}$
$J = \frac{P_t}{K_f K_u B_{ac} f A_p}$	$L = \frac{0.4\pi N^2 A_c F 10^{-7}}{l_g}$
$A_p = W_a A_c$	$F = 1 + \frac{l_g}{\sqrt{A_c}} Ln\left(\frac{2G}{l_g}\right)$

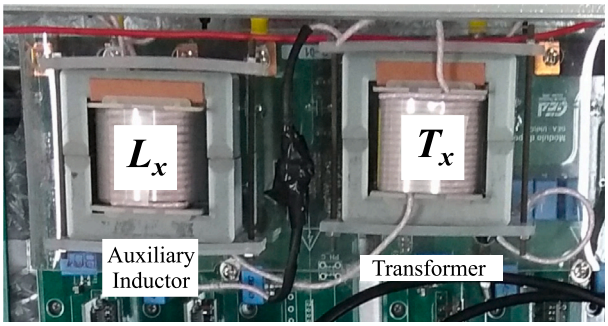

Fig. 6. Photograph of the transformer and auxiliary inductor of the DAB x module.

4.2. Results using a unique modulator

Fig. 7 shows the steady-state experimental measurements of the DC port voltages V_{xy}, the input and output currents I_y, the powers P_x transferred by each DAB module and the power P_o transferred by the modular converter when a unique modulator is used. These experimental measurements are compared with the theoretical values (continuous or dashed line) predicted by the model using the Eqs. (18) to (21). In this figure, the experimental measurements of the DAB modules DAB 1, DAB 2, and DAB 3 are represented by the ◇, ×, and ▽ marks, respectively. For this operating condition, it is fulfilled that the DC voltages of each module are set at different values as predicted by the model, obtaining the following relationships for the implemented converter: $V_{31} < V_{11} < V_{21}$ and $V_{32} < V_{12} < V_{22}$, since $L_3 < L_1 < L_2$. Although each module has different DC voltages, the experimental results validate that the condition $d_1 = d_2 = d_3$ is satisfied.

4.2.1. Parametric sensitivity analysis

From the steady-state model presented in Section 3.1, it is possible to analyze the parametric sensitivity of the DC port voltages of the modular converter modules as a function of the leakage inductances of the experimental prototype when L_1 is set as the nominal value. Assuming a modular converter case A with three equal DAB modules ($L_1 = L_2 = L_3$), it is possible to establish by Eq. (18) the following relationship between the voltages $V_{xy,A}$,

$$V_{1y,A} = V_{2y,A} = V_{3y,A} = \frac{V_{y,A}}{3}, \tag{27}$$

that is satisfied at all operating points of the modular converter.

On the other hand, in the modular converter with parametric differences in the leakage inductances, there is an imbalance in the voltages V_{xy} of the DC ports, as established by Eq. (18). Being L_1 the nominal inductance, it is possible to establish a percentage variation's range for L_2 and L_3 and to obtain the maximum voltage deviation $\Delta V_{xy,max}$ expressed in (pu) concerning case A at each point of that range. This analysis allows plotting $\Delta V_{xy,max}$ (pu) using contour lines as shown in Fig. 8, where the variation of the inductances L_2 and L_3 is also expressed in (pu) concerning the nominal inductance. From the results presented in this figure, it is possible to establish a maximum voltage deviation $\Delta V_{xy,max}$ allowed in an application, and the corresponding contour line considers all possible combinations of allowable parametric variations.

Case B corresponds to the experimental prototype identified in Fig. 8 by the red ∗ mark and has the following percentage variation among the leakage inductances,

$$\begin{aligned} L_1 &= 140\ \mu\text{H} \\ L_2 &= L_1 + 17,09\%L_1 \\ L_3 &= L_1 - 6,54\%L_1 \end{aligned} \tag{28}$$

as can be seen in Table 1. Such parametric variation in the leakage inductances implies a variation in the DC port voltages, obtained by Eq. (18), resulting,

$$\begin{aligned} V_{1y,B} &= \frac{V_y}{3} - 3,4\%V_{xy,A} \\ V_{2y,B} &= \frac{V_y}{3} + 13,1\%V_{xy,A} \\ V_{3y,B} &= \frac{V_y}{3} - 9,7\%V_{xy,A} \end{aligned} \tag{29}$$

where the percentage voltage variation is expressed concerning case A of a modular converter consisting of three equal DAB modules with a voltage $V_{xy,A}$ in each module, Eq. (27).

The sensitivity to parametric variations, particularly in the leakage inductances L_x of DAB module transformers, directly affects real-world applications. In particular, applications such as MV microgrids, electric vehicles, or SSTs require reliable operation under varying conditions, including load and voltage fluctuations. The ability of the modular converter to maintain optimal performance in the face of these variations translates into lower maintenance costs and a longer system lifetime. Therefore, the results in Fig. 6 show that voltage deviations are due to differences in the leakage inductances of the modules, and consequently, it is important to incorporate robust design techniques and modulation strategies that mitigate these effects.

4.2.2. Evaluation of soft-switching operation

The experimental measurements in Fig. 7 can be plotted in a nomogram, as shown in Fig. 9, to evaluate the ZVS operation of the modular converter. The output current of each DAB module normalized for its base current, and using Eq. (9), can be expressed as,

$$I_{Bx2}(pu) = \frac{I_{Bx2}}{V_{x1}/(\omega L_x)} = \frac{I_2}{V_{x1}/(\omega L_x)}. \tag{30}$$

From Eqs. (17) and (30), it follows that $I_{B12}(pu) = I_{B22}(pu) = I_{B32}(pu)$. Therefore, applying the conditions established in Section 3.3, it is determined that all modules will operate with hard-switching (HS) or all with ZVS, depending on the phase shift applied, as shown in the nomogram.

Fig. 10 shows the results of Test 1 in boost mode using a unique modulator when the phase shift $\Delta = 70°$ is applied. Fig. 10(a) shows the experimental waveforms of the voltage v_{T11}, and the currents i_{L1}, i_{L2} and i_{L3} of the auxiliary inductors used in Test 1. In these current waveforms, the □ mark is used to indicate the instantaneous value of $i_{Lx}(\Delta_x)$, and the ∘ mark is used for $i_{Lx}(\pi)$. These instantaneous values are shown in green and red when the current's sign is positive and negative, respectively. The figure shows that $i_{Lx}(\Delta) > 0$ and $i_{Lx}(\pi) > 0$, which means that all DAB modules operate with ZVS. This operating point in boost mode corresponds to the result identified as Test 1 in the nomogram of Fig. 9. Fig. 10(b) shows the voltages V_{x2} of the output DC ports of the modular converter corresponding to Test 1. This figure allows the model to be validated since applying the same phase shift to all the modules results in an imbalance in the voltages V_{x2} which depends on the magnitudes of the leakage inductances, as established by Eq. (18).

Fig. 11 presents the results of Test 2 in buck mode using a unique modulator when the phase shift $\Delta = 10°$ is applied. Fig. 11(a) shows

Table 4
Parameters of the implemented magnetic components.

Module	L_x	Transformers' parameters			Inductors' parameters		
		Turns (1:1)	Magnetizing inductance	Leakage inductance	Turns	Inductance	Air-gap
DAB 1	140 μH	15	817 μH	3.45 μH	12	136.55 μH	1.05 mm
DAB 2	163.92 μH	15	885 μH	3.56 μH	13	160.36 μH	1.06 mm
DAB 3	130.85 μH	15	857 μH	3.51 μH	13	127.34 μH	1.37 mm

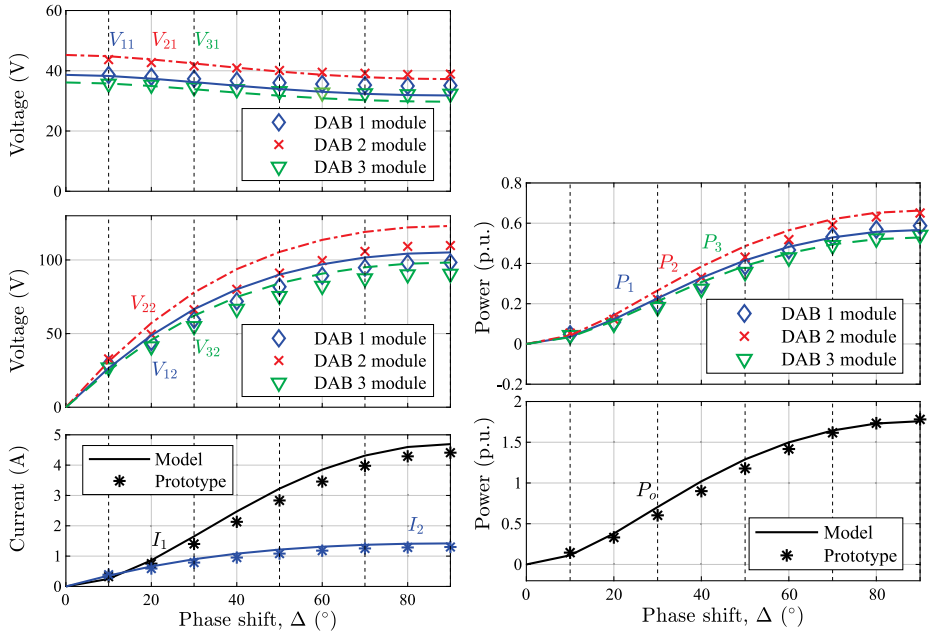

(a) DC voltages and currents. (b) Power transferred.

Fig. 7. Magnitudes V_{xy}, I_y, P_x and P_o in steady state for $\Delta_1 = \Delta_2 = \Delta_3$.

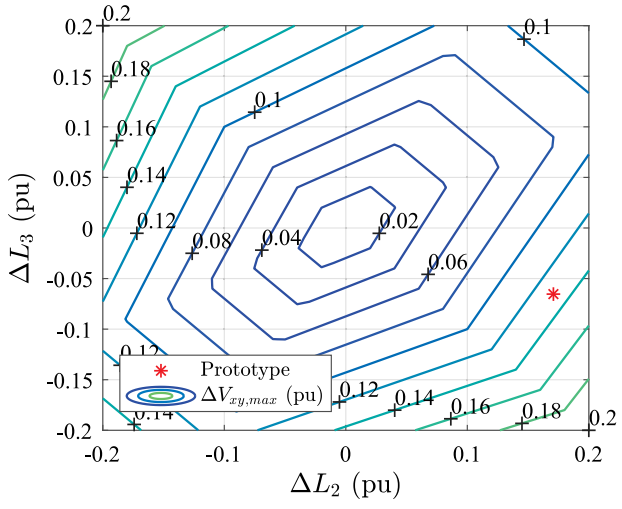

Fig. 8. Maximum voltage variation $\Delta V_{xy,max}$ (pu) of the DAB modules with parametric variation in the leakage inductances, concerning case A with three equal modules and a unique modulator.

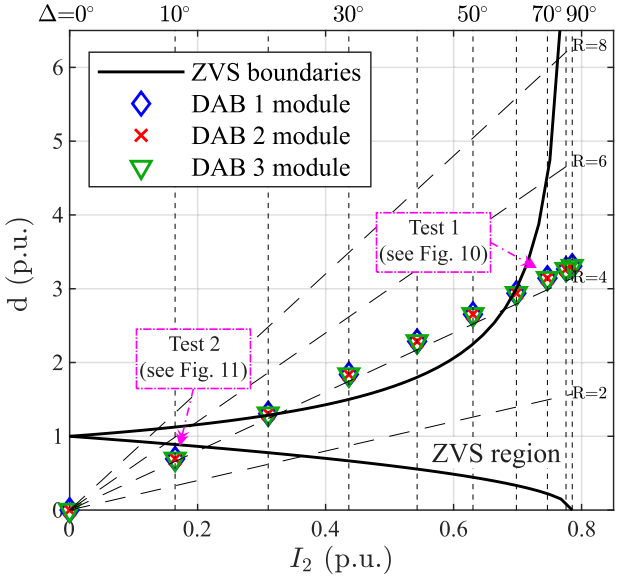

Fig. 9. Nomogram for $\Delta_1 = \Delta_2 = \Delta_3$.

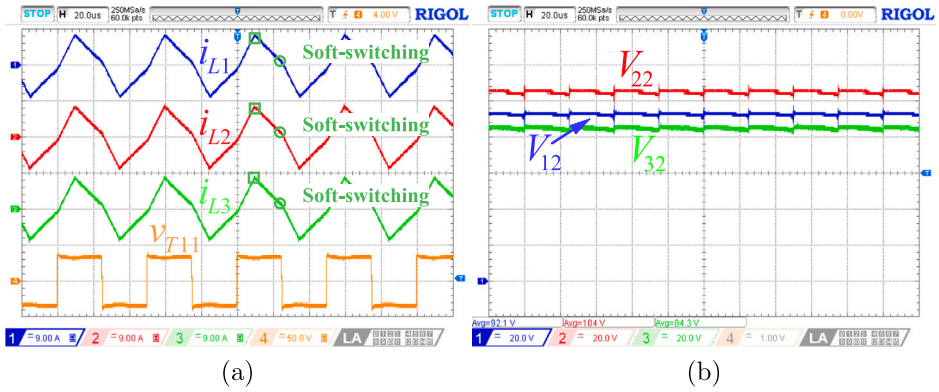

Fig. 10. Test 1: Voltage and current waveforms for $\Delta = 70°$, in boost mode. Vertical scales (a): CH1(i_{L1})=9 A/div; CH2(i_{L2})=9 A/div; CH3(i_{L3})=9 A/div; CH4(v_{T11})=50 V/div. Vertical scales (b): CHx(V_{x2})=20 V/div. (For interpretation of the references to color in this figure legend, the reader is referred to the web version of this article.)

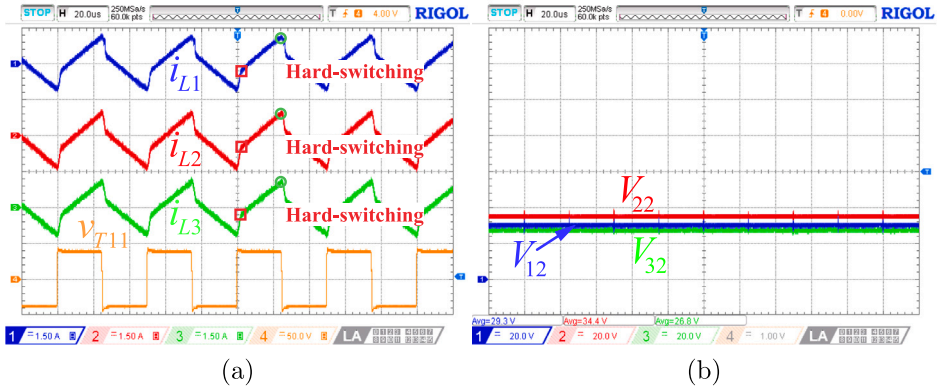

Fig. 11. Test 2: Voltage and current waveforms for $\Delta = 10°$, in buck mode. Vertical scales (a): CH1(i_{L1})=1.5 A/div; CH2(i_{L2})=1.5 A/div; CH3(i_{L3})=1.5 A/div; CH4(v_{T11})=50 V/div. Vertical scales (b): CHx(V_{x2})=20 V/div.

the experimental waveforms of the voltage v_{T11}, and the currents i_{L1}, i_{L2} and i_{L3} of the auxiliary inductors in Test 2. The figure shows that $i_{Lx}(\Delta) < 0$ and $i_{Lx}(\pi) > 0$, which means that all DAB modules operate under hard-switching mode. This operating point in buck mode corresponds to the result identified as Test 2 in the nomogram of Fig. 9. Fig. 11(b) shows the voltages V_{x2} when the phase shift $\Delta = 10°$ is applied. This figure allows the model to be validated since applying the phase shift $\Delta = 10°$ to all the modules results in an imbalance in the voltages V_{x2} which depends on the magnitudes of the leakage inductances, as established by Eq. (18). In the experimental prototype, the module DAB 2 has the largest leakage inductance and, consequently, the highest DC voltage at its terminals when using a unique modulator.

4.3. Results using independent modulators

Fig. 12 shows the steady-state experimental measurements of the DC port voltages V_{xy}, the input and output currents I_y, the powers P_x transferred by each DAB module, and the total power P_o transferred by the modular converter when the necessary phase shifts are applied to each module to achieve a balanced voltage distribution. These experimental measurements are compared with the theoretical values (continuous or dashed line) predicted by the model through the Eqs. (23)–(26). It can be observed that, although $L_3 < L_1 < L_2$, it is possible to establish phase shifts Δ_x that satisfy the expression (23), yielding $V_{11} = V_{21} = V_{31}$ and $V_{12} = V_{22} = V_{32}$. In this case, where $L_3 < L_1 < L_2$, for each operating point with $0 < \Delta_2 < \pi/2$ rad, the corresponding phase shifts Δ_1 and Δ_3 that balance the voltages V_{xy} are calculated using Eq. (23).

4.3.1. Evaluation of soft-switching operation

Similar to the previous case, to evaluate the switching condition of each module, the experimental measurements in Fig. 12 are plotted on a nomogram applying the conditions presented in Section 3.3, as shown in Fig. 13. The output current of each module normalized concerning its base current and using the Eqs. (9) and (25), is expressed as,

$$I_{Bx2}(pu) = \frac{I_{Bx2}}{V_{x1}/(\omega L_x)} = \frac{I_2}{V_1/(3\omega L_x)}, \tag{31}$$

and it can be observed that $I_{B12}(pu) \neq I_{B22}(pu) \neq I_{B32}(pu)$. Applying these relations and the conditions presented in Section 3.3 it is established that at certain d_x the DAB module 2 operates with ZVS, while the DAB modules 1 and 3 operate in HS, as seen in this figure.

Fig. 14 shows the results of Test 3 in boost mode using independent modulators corresponding to $\Delta_1 = 51°$, $\Delta_2 = 70°$, and $\Delta_3 = 46°$. Fig. 10(a) shows the experimental waveforms of the voltage v_{T11}, and the currents i_{L1}, i_{L2} and i_{L3} of the auxiliary inductors in Test 3. It can be observed that $i_{L1}(\pi) < 0$, $i_{L2}(\pi) > 0$, and $i_{L3}(\pi) < 0$; therefore, DAB module 2 is in ZVS, while DAB modules 1 and 3 are in HS. This result in boost mode corresponds to the result identified as Test 3 in the nomogram in Fig. 13 for Test 3. Fig. 14(b) shows the voltages V_{x2} when the phase shifts $\Delta_1 = 51°$, $\Delta_2 = 70°$, and $\Delta_3 = 46°$ are applied. This figure allows the model to be validated since applying the phase shifts that it is established by Eq. (24) results in a quasi-balance condition in the voltages V_{x2}. In a real-world implementation, there is a certain inaccuracy in the determination of leakage inductances. Consequently, there is a small imbalance between the voltages V_{x2} by the modules when the theoretical phase shifts are applied.

Fig. 15 shows the results of Test 4 in buck mode using independent modulators corresponding to $\Delta_1 = 17°$, $\Delta_2 = 20°$, and $\Delta_3 = 16°$.

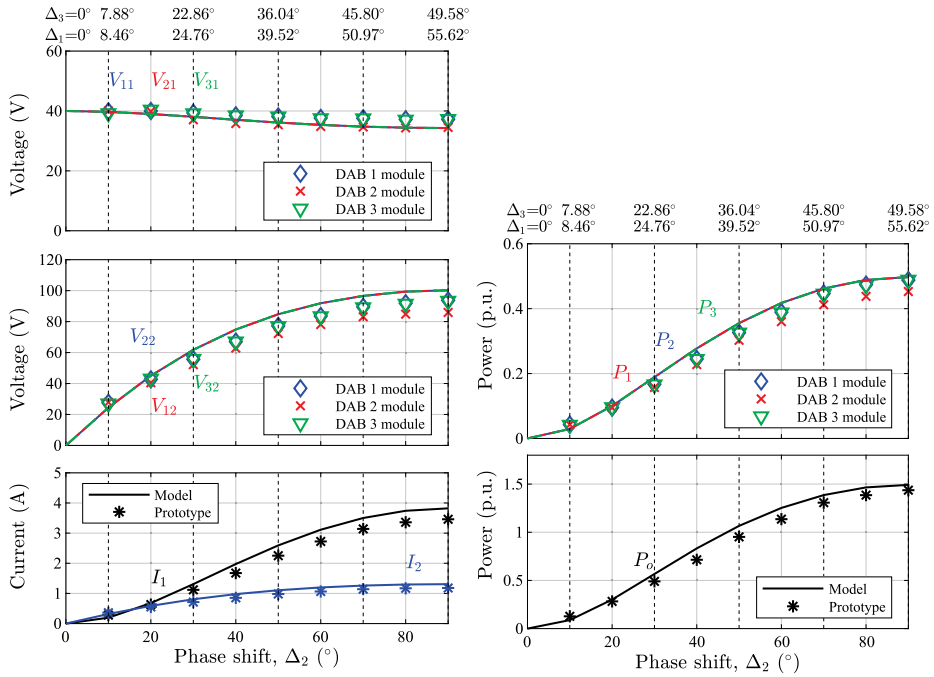

Fig. 12. Magnitudes V_{xy}, I_y, P_x and P_o in steady state for $\Delta_1 \neq \Delta_2 \neq \Delta_3$.

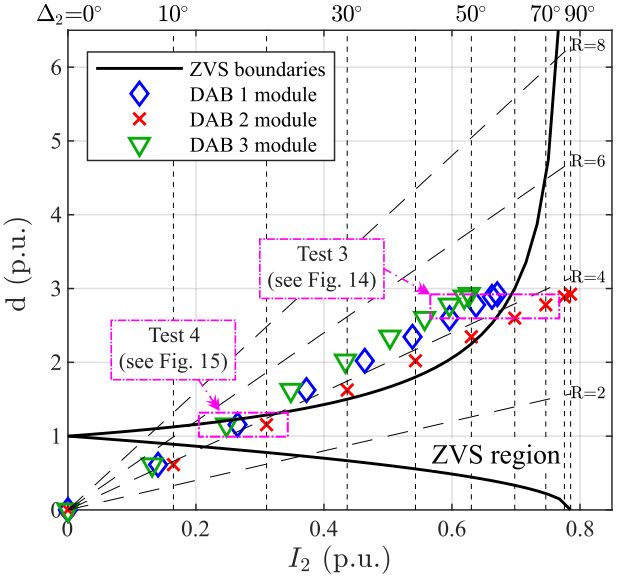

Fig. 13. Nomogram for $\Delta_1 \neq \Delta_2 \neq \Delta_3$.

Fig. 15(a) shows the experimental waveforms of the voltage v_{T11}, and the currents i_{L1}, i_{L2} and i_{L3} of the auxiliary inductors in Test 4. It can be observed that $i_{Lx}(\Delta_x) > 0$ and $i_{Lx}(\pi) > 0$, which means that all DAB modules operate with ZVS. This test in buck mode corresponds to the result identified as Test 4 in the nomogram of Fig. 13. Fig. 15(b) shows the balanced voltages V_{x2} when the phase shifts $\Delta_1 = 17°$, $\Delta_2 = 20°$, and $\Delta_3 = 16°$ are applied.

4.3.2. Analysis of the soft-switching region for the modular converter

The soft-switching restrictions presented by Eqs. (6) and (7) allow each DAB module's hard or soft-switching condition to be analyzed. However, the modular converter with independent modulators operates with soft-switching when all DAB modules operate with ZVS. Therefore, from the nomogram and the experimental results presented in this section, it is possible to conclude that using independent modulators to balance the voltages V_{xy} changes the ZVS region of the modular converter.

Considering that in the experimental prototype $L_3 < L_1 < L_2$, then the operating point at the boundary of the ZVS region for the modular converter is obtained when $\Delta_{3,lim}$ satisfies the equality in Eq. (6) or (7), in buck or boost mode, respectively. Then, from the magnitude of $\Delta_{3,lim}$ and Eq. (23), $\Delta_{1,lim}$ and $\Delta_{2,lim}$ can be obtained, which balance the voltages V_{xy} of the DC ports of the modular converter operating with ZVS for the limiting case posed. Fig. 16 presents the boundary of the ZVS region of each DAB module corresponding to a theoretical parametric variation of 10% in the leakage inductances under the operation condition with balanced V_{xy} voltages. Therefore, from the ZVS region limits presented in this figure, it is possible to conclude that by using independent modulators to balance the V_{xy} voltages of the DC ports, the ZVS region of the modular converter is reduced due to the parametric variation in the leakage inductances of the modules. Furthermore, in the analysis of this figure, it should be noted that the operating region of the modular converter is limited to a maximum phase shift $\Delta_{2,max} = 90°$, as indicated by a dashed red vertical line. Therefore, it is important to evaluate the region of operation with ZVS when using independent modulators, considering the efficiency required according to the specific application.

4.4. Comparison results using both strategies

Fig. 17 shows the efficiency, η, of the modular converter as a function of the normalized output power, P_o. These results correspond to the power transferred using both unique modulator and independent modulators, presented in Fig. 7(b) and Fig. 12(b), respectively. As can be observed in this figure, the efficiency of the modular converter is similar using both methods. This test allows to conclude that the decrease in the ZVS operating region using independent modulators does not significantly affect the overall efficiency. When a single modulator is used, it is possible to apply the maximum phase shift $\Delta_{x,max} = 90°$

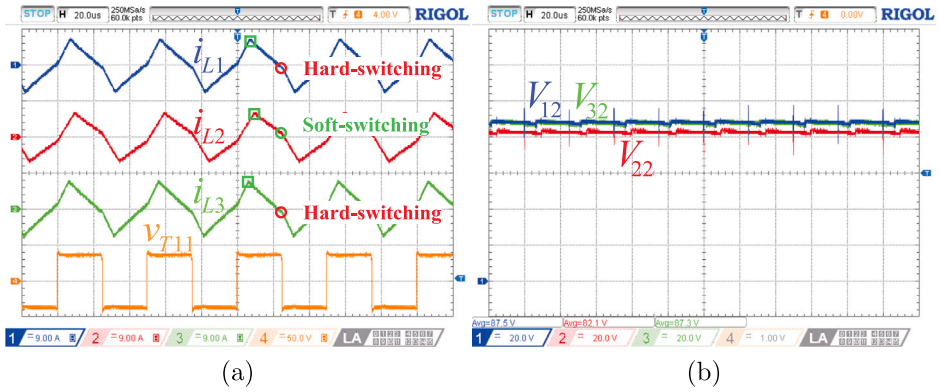

Fig. 14. Test 3: Voltage and current waveforms for $\Delta_1 = 51°$, $\Delta_2 = 70°$ *y* $\Delta_3 = 46°$, in boost mode. Vertical scales (a): CH1(i_{L1})=9 A/div; CH2(i_{L2})=9 A/div; CH3(i_{L3})=9 A/div; CH4(v_{T11})=50 V/div. Vertical scales (b): CHx(V_{x2})=20 V/div.

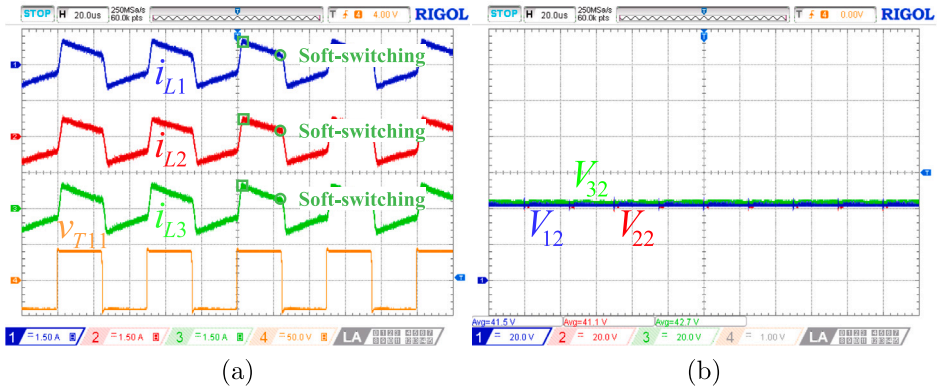

Fig. 15. Test 4: Voltage and current waveforms for $\Delta_1 = 17°$, $\Delta_2 = 20°$ and $\Delta_3 = 16°$, in buck mode. Vertical scales (a): CH1(i_{L1})=1.5 A/div; CH2(i_{L2})=1.5 A/div; CH3(i_{L3})=1.5 A/div; CH4(v_{T11})=50 V/div. Vertical scales (b): CHx(V_{x2})=20 V/div.

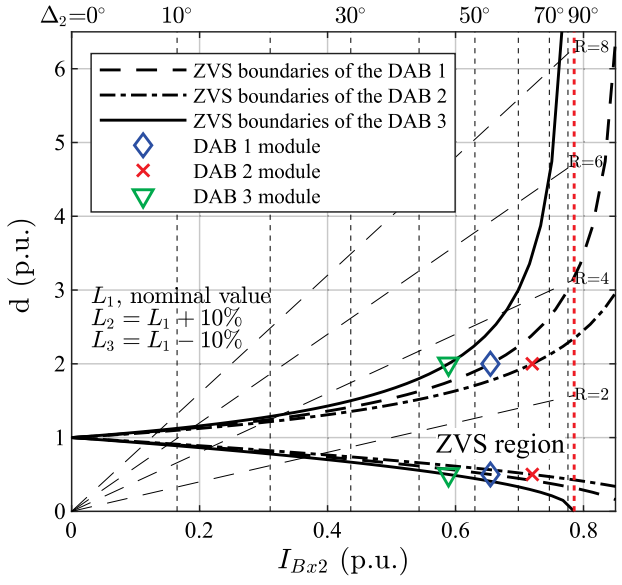

Fig. 16. Nomogram for $\Delta_1 \neq \Delta_2 \neq \Delta_3$ with L_1 as the nominal value, $L_2 = L_1 + 10\%L_1$, and $L_3 = L_1 - 10\%L_1$. (For interpretation of the references to color in this figure legend, the reader is referred to the web version of this article.)

to all modules. As a result, maximum power to the load is transferred with respect to the one obtained for the method using independent modulators. This condition can be explained by the fact that the same phase shift controls the power transferred by each DAB module Δ_x, as expressed in Eq. (4). Instead, when independent modulators are used and $\Delta_{2,max}$ is applied to DAB module 2, corresponding to the largest leakage inductance for the case study ($L_3 < L_1 < L_2$), whereas the phase shifts applied to the remaining modules satisfying the condition (24) such that $\Delta_3 < \Delta_1 < \Delta_2$, then the maximum power transferred to the load is lower than in the case using a unique modulator.

Finally, the analysis presented in this article and the comparison of the results obtained allow the flowchart shows in Fig. 18 to be proposed, which presents a guide to select the topology of the power converters according to the requirements of the MVDC microgrids. It should be noted that all topologies indicated in this flowchart are included in the bibliography and discussed in the Introduction of this paper. From this flowchart, it is possible to establish the strategy to be used to control the power flow of the DAB modules in MVDC microgrids. The parametric analysis shown in Fig. 8 demonstrates that a parametric variation, for example, less than 5% in the size of L_x, produces an imbalance of voltage less than 5%, allowing the use of a unique modulator. In the opposite case, where the tolerance in the L_x is greater than 5%, independent modulators should be used to balance the voltages V_{xy}.

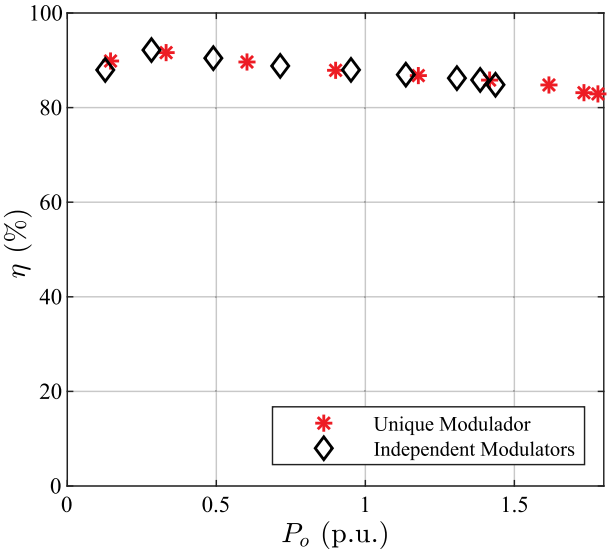

Fig. 17. Efficiency comparison between unique modulator and independent modulator's methods.

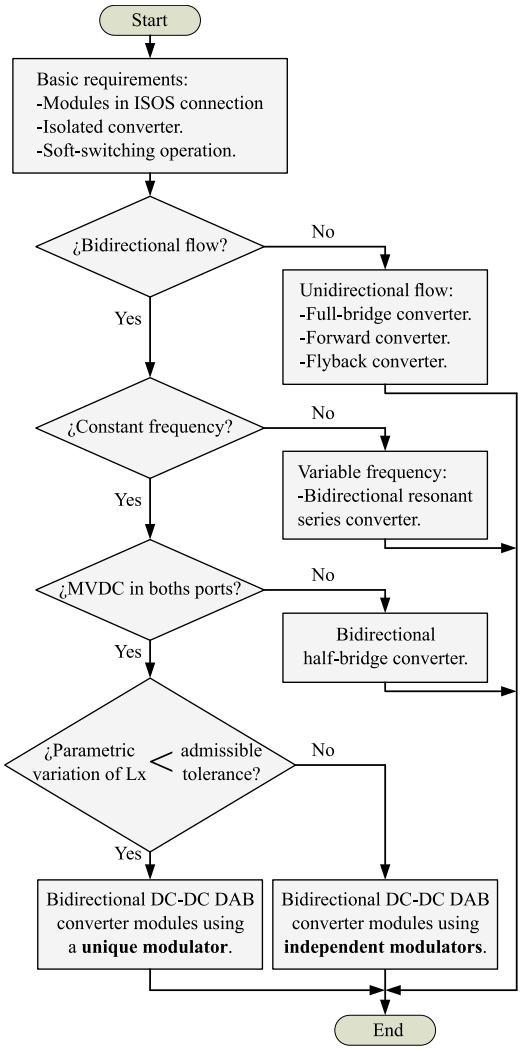

Fig. 18. Flowchart used as a guide to select the ISOS converter topology for MVDC microgrid applications.

4.5. Comparison with other authors' proposals

Table 5 presents a comparison with other modular converters presented in the literature, considering the main parameters and characteristics of the proposed modular converter (MC). In this table, the MC-year notation is used to identify the publication year of each of the Refs. [6,24–27], respectively, whose authors have proposed different modular converters using DAB modules. As can be observed, the MC proposed in this article contemplates the existing parametric differences between the DAB modules in the model and establishes the admissible parametric difference in the leakage inductances for a given voltage unbalance between the modules that allow the use of a unique modulator. In addition, this work determines the ZVS conditions of each module and the ZVS operating region when using a unique or independent modulator.

5. Conclusions

This paper presented an analysis for connecting DAB converter modules in series at the input and output ports, forming a modular converter for medium voltage DC microgrid applications. Power transfer in this modular converter can be accomplished by using a unique modulator and independent modulators applied to each DAB module. The steady-state model of the system establishes the voltage distribution between the modules and the transferred power, depending on the DAB modules' parameters.

For the two proposed power transfer control methods, the soft-switching regions of the modular converter were analyzed as a function of the parameters and operating points of each DAB module. This analysis led to the conclusion that, in the case of using a unique modulator, simplicity of the power transfer control of the modular converter is obtained, and all modules have the same operating condition with hard or soft-switching over the entire operating range. This method, which uses a unique modulator, is implementable in applications that allow a determined imbalance in the DC port voltages due to the existing parametric variations between the DAB modules. When using independent modulators, the phase shifts can be set to balance the DC port voltages of the modular converter, balancing the powers transferred by the DAB modules. The disadvantage of this operating condition is that the ZVS operating region of the modular converter is reduced because there are operating points where one module may operate with soft-switching while others operate with hard-switching. Future work aims to evaluate advanced modulation strategies to extend the ZVS operating region of the modular converter. In addition, using independent modulators, the maximum power that the modular converter can transfer is lower than using a unique modulator established by the module with the largest leakage inductance.

Finally, the experimental results of the two cases analyzed were presented to validate the theoretical analysis. The analysis performed in a normalized domain, independently of the specific parameters of the implemented experimental prototype, can be extended to different power and voltage levels. Nowadays, commercially available high-voltage (HV) semiconductor devices (such as high-voltage silicon carbide (SiC) MOSFETs [28]), are candidates for implementing conventional topologies using the same modulation techniques and control strategies. Therefore, despite the results presented in this paper using a scaled-down prototype, the conclusions could be scalable to higher power levels typical of a medium-voltage DC microgrid by extending the analysis and results presented in this paper.

Table 5
Comparison of the proposal with other references that include experimental results.

Reference	MC-2015	MC-2017	MC-2019	MC-2022	MC-2023	MC proposed
Type of connection	ISOS	ISOP	IPOS	Hybrid ISOS	ISOP	ISOS
Topology	DAB	DAB	DAB	SR-DAB & DAB with LC branch	DAB	DAB
Modulators	Unique modulator	Independent modulators	Independent modulators	Unique modulator	Independent modulators	Unique & Indep. Mod.
Modulation strategy utilized	SPS	TPS	SPS	SPS	TPS	SPS
Modeling considering parametric differences	No	No	No	No	No	Yes
Assessment of the parametric variation	No	No	No	No	No	Yes
Determination of ZVS operating region	No	No	No	No	No	Yes
Determination of ZVS conditions in each module	No	No	No	No	No	Yes
Rated power	400 W	4.5 kW	1.25 kW	600 W	600 W	500 W
N° of modules	2	3	2	3	3	3
Parametric differences in the prototype (%)	No	Yes (%N/A)	Yes (20% in L_x)	No	Yes (40% in L_x)	Yes (17% in L_x)
V_{in}	400 V	720 V	100 V	150 V	150 V	120 V
V_{out}	400 V	380 V	100 V	150 V	50 V	300 V
f_s	40 kHz	20 kHz	5 kHz	10 kHz	20 kHz	20 kHz

CRediT authorship contribution statement

D. Garrido: Writing – review & editing, Writing – original draft, Visualization, Validation, Software, Methodology, Investigation, Funding acquisition, Formal analysis, Data curation, Conceptualization. **F. Rodríguez:** Writing – original draft, Software, Investigation, Funding acquisition, Data curation. **J. Bosso:** Writing – review & editing, Supervision, Resources, Project administration, Conceptualization. **G. Oggier:** Writing – review & editing, Writing – original draft, Supervision, Resources, Project administration, Investigation, Conceptualization.

Declaration of competing interest

The authors declare the following financial interests/personal relationships which may be considered as potential competing interests: G. Oggier reports financial support was provided by the National Agency for Scientific and Technological Promotion in Argentina. If there are other authors, they declare that they have no known competing financial interests or personal relationships that could have appeared to influence the work reported in this paper.

Data availability

Data will be made available on request.

References

[1] G.P. Adam, I.A. Gowaid, S.J. Finney, D. Holliday, B.W. Williams, Review of DC-DC converters for multi-terminal HVDC transmission networks, IET Power Electron. 9 (2) (2016) 281–296, http://dx.doi.org/10.1049/iet-pel.2015.0530.

[2] K. Vechalapu, S. Bhattacharya, Performance comparison of 10 kV-15 kV high voltage SiC modules and high voltage switch using series connected 1.7 kV LV SiC MOSFET devices, in: 2016 IEEE Energy Convers. Congr. and Expo., ECCE, 2016, pp. 1–8, http://dx.doi.org/10.1109/ECCE.2016.7855343.

[3] F. Briz, M. López, A. Rodríguez, M. Arias, Modular power electronic transformers: Modular multilevel converter versus cascaded H-bridge solutions, IEEE Ind. Electron. Mag. 10 (4) (2016) 6–19, http://dx.doi.org/10.1109/MIE.2016.2611648.

[4] M. ElMenshawy, A. Massoud, Development of modular DC-DC converters for low-speed electric vehicles fast chargers, Alex. Eng. J. 60 (1) (2021) 1067–1083, http://dx.doi.org/10.1016/j.aej.2020.10.031.

[5] D. Ma, W. Chen, X. Ruan, A review of voltage/current sharing techniques for series-parallel-connected modular power conversion systems, IEEE Trans. Power Electron. 35 (11) (2020) 12383–12400, http://dx.doi.org/10.1109/TPEL.2020.2984714.

[6] S. Lee, Y.C. Jeung, D.C. Lee, Voltage balancing control of IPOS modular dual active bridge DC/DC converters based on hierarchical sliding mode control, IEEE Access 7 (2019) 9989–9997, http://dx.doi.org/10.1109/ACCESS.2018.2889345.

[7] L. Qu, D. Zhang, B. Zhang, Input voltage sharing control scheme for input series and output parallel connected DC-DC converters based on peak current control, IEEE Trans. Ind. Electron. 66 (1) (2019) 429–439, http://dx.doi.org/10.1109/TIE.2018.2829691.

[8] A.J.B. Bottion, I. Barbi, Input-series and output-series connected modular output capacitor full-bridge PWM DC-DC converter, IEEE Trans. Ind. Electron. 62 (10) (2015) 6213–6221, http://dx.doi.org/10.1109/TIE.2015.2424204.

[9] D. Sha, Z. Guo, T. Luo, X. Liao, A general control strategy for input-series–output-series modular DC–DC converters, IEEE Trans. Power Electron. 29 (7) (2014) 3766–3775, http://dx.doi.org/10.1109/TPEL.2013.2278546.

[10] M.A. Pagliosa, T.B. Lazzarin, R.G. Faust, I. Barbi, Input-series and output-series connected modular single-switch flyback converter operating in the discontinuous conduction mode, IET Power Electron. 9 (9) (2016) 1962–1970, http://dx.doi.org/10.1049/iet-pel.2015.0935.

[11] M.A. Alam, A.F. Minai, F.I. Bakhsh, Isolated bidirectional DC-DC Converter: A topological review, e-Prime - Adv. Electr. Eng. Electron. Energy 8 (April) (2024) 100594, http://dx.doi.org/10.1016/j.prime.2024.100594.

[12] F. Krismer, Modeling and Optimization of Bidirectional Dual Active Bridge DC – DC Converter Topologies (Ph.D. thesis), (19177) ETH ZURICH, 2010.
[13] O.M. Ghazal, M.I. Marei, A.M. Mohamad, Small-signal modeling comparison of dual active bridge converter, e-Prime - Adv. Electr. Eng. Electron. Energy 8 (April) (2024) 100570, http://dx.doi.org/10.1016/j.prime.2024.100570.
[14] K. Zhang, Z. Shan, J. Jatskevich, Large- and small-signal average-value modeling of dual-active-bridge DC–DC converter considering power losses, IEEE Trans. Power Electron. 32 (3) (2017) 1964–1974, http://dx.doi.org/10.1109/TPEL.2016.2555929.
[15] F. Rodríguez, D. Garrido, R. Núñez, G.G. Oggier, G.O. García, Modelado dinámico y de estado estacionario para la conexión modular entrada serie - salida serie de convertidores con puentes duales activos, Rev. Iberoam. Autom. Inf. Ind. 18 (4) (2021) 371–384, http://dx.doi.org/10.4995/riai.2021.14866.
[16] R.W.A.A. De Doncker, D.M. Divan, M.H. Kheraluwala, A three-phase soft-switched high-power-density DC/DC converter for high-power applications, IEEE Trans. Ind. Appl. 27 (1) (1991) 63–73, http://dx.doi.org/10.1109/28.67533.
[17] M.H. Kheraluwala, R.W. Gascoigne, D.M. Divan, E.D. Baumann, Performance characterization of a high-power dual active bridge dc-to-dc converter, IEEE Trans. Ind. Appl. 28 (6) (1992) 1294–1301, http://dx.doi.org/10.1109/28.175280.
[18] G.G. Oggier, R. Leidhold, G.O. García, A.R. Oliva, J.C. Balda, F. Barlow, Extending the ZVS operating range of dual active bridge high-power DC-DC converters, in: PESC Record - IEEE Annual Power Electron. Specialists Conf., 2006, pp. 2–8, http://dx.doi.org/10.1109/PESC.2006.1712142.
[19] G. Oggier, Control para minimizar las pérdidas en convertidores CC-CC con puentes duales activos (Ph.D. thesis), Univ. Nac. del Sur, Fac. de Ing., Bahía Blanca, Argentina, 2009, Tesis de Doctorado en Control de Sistemas.
[20] C.W.T. McLyman, Transformer and Inductor Design Handbook, fourth ed., CRC Press, 2011, pp. 7–1–7–30, 10–1–10–13.
[21] I. Villar, U. Viscarret, I. Etxeberria-Otadui, A. Rufer, Global loss evaluation methods for nonsinusoidally fed medium-frequency power transformers, IEEE Trans. Ind. Electron. 56 (10) (2009) 4132–4140, http://dx.doi.org/10.1109/TIE.2009.2021174.
[22] PRYDE, Ferrite Núcleo E 70/33/32, 2022, URL http://www.pryde.com.ar/ficha.php?s=8&c=&g=64&p=987.
[23] NEWT, New England wire technologies (NEWT) home page, 2025, URL https://www.newenglandwire.com/.
[24] A.J. Bento Bottion, I. Barbi, Series-series association of two dual active bridge (DAB) converters, in: Proceedings of the IEEE International Conference on Industrial Technology, vol. 2015-June, (June) 2015, pp. 1161–1166, http://dx.doi.org/10.1109/ICIT.2015.7125254.
[25] B. Zhao, Q. Song, J. Li, Q. Sun, W. Liu, Full-process operation, control, and experiments of modular high-frequency-link DC transformer based on dual active bridge for flexible MVDC distribution: A practical tutorial, IEEE Trans. Power Electron. 32 (9) (2017) 6751–6766, http://dx.doi.org/10.1109/TPEL.2016.2626262.
[26] C. Sun, X. Zhang, J. Zhang, M. Zhu, J. Huang, Hybrid input-series-output-series modular DC-DC converter constituted by resonant and nonresonant dual active bridge modules, IEEE Trans. Ind. Electron. 69 (1) (2022) 1062–1069, http://dx.doi.org/10.1109/TIE.2021.3055175.
[27] Y. Zeng, J. Pou, C. Sun, S. Mukherjee, X. Xu, A.K. Gupta, J. Dong, Autonomous input voltage sharing control and triple phase shift modulation method for ISOP-DAB converter in DC microgrid: A multiagent deep reinforcement learning-based method, IEEE Trans. Power Electron. 38 (3) (2023) 2985–3000, http://dx.doi.org/10.1109/TPEL.2022.3218900.
[28] R.A. Gomez, D.A. Porras, G.G. Oggier, J.C. Balda, Y. Zhao, A three-phase isolated building block for high-power medium-voltage grid applications, IEEE J. Emerg. Sel. Top. Power Electron. 12 (2) (2024) 1324–1336, http://dx.doi.org/10.1109/JESTPE.2023.3311775.

Daniel O. Garrido was born in Zapala, Argentina. He received the degree of Electronic Engineer from the Universidad Nacional del Comahue, Neuquén, Argentina, in 2018, and the doctor of engineering sciences degree from the Universidad Nacional de Río Cuarto, Río Cuarto, Argentina, in 2024. In 2018, he joined the Grupo de Electrónica Aplicada, Facultad de Ingeniería, Universidad Nacional de Río Cuarto, where he is currently a Professor and a post-doctoral fellow at the Consejo Nacional de Investigaciones Científicas y Técnicas (CONICET), Argentina. His current research interests include the solid-state transformer, power electronics, and renewable energy conversion.

Federico Rodríguez was born in Neuquén, Neuquén, Argentina, in 1989. He received the Electronic Engineering degree from the Universidad Nacional del Comahue (UNComa), Neuquén, Argentina, in 2017. He is a Doctoral Fellow in the Grupo de Electrónica Aplicada, Instituto de Investigaciones en Tecnologías Energéticas y Materiales Avanzados, Universidad Nacional de Río Cuarto. His research interests include power electronics, renewable energy conversion and modular power converters.

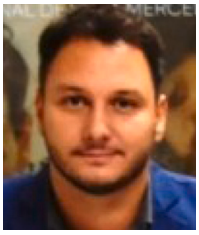

Jonathan E. Bosso was born in Villa Mercedes, Argentina, in 1986. He received the electronics engineering degree from the Universidad Nacional de San Luis (UNSL), Argentina, in 2012 and the doctor of engineering sciences degree from the Universidad Nacional de Rio Cuarto (UNRC), Argentina, in 2017. Since 2007, he is a member of Laboratorio de Control Automático, UNSL, and from 2012, he joined the Grupo de Electrónica Aplicada, UNRC. He is also with the Consejo Nacional de Investigaciones Cientificas y Técnicas (CONICET), Argentina. He has extensive experience in academia, having taught at various institutions, including the UNSL, UNRC and National University of Villa Mercedes (UNViMe), where he also served as Secretary of Science, Technology, and Technological Linkage. His research primarily revolves around power converters and renewable energy integration, evidenced by numerous projects and publications. Additionally, he has actively contributed to scientific innovation and extension projects, securing significant funding and collaborating on high-impact technological initiatives.

Germán G. Oggier was born in Cordoba, Argentina. He received the Electr. Eng. degree and the M.Sc. degree in electrical engineering from the Universidad Nacional de Rio Cuarto, Rio Cuarto, Argentina, in 2003 and 2006, respectively, and the Doctor degree in control systems from the Universidad Nacional del Sur, Buenos Aires, Argentina, in 2009. In 1999, he joined the Grupo de Electrónica Aplicada, Facultad de Ingeniería, Universidad Nacional de Río Cuarto, where he is currently a Professor and a Researcher at the Consejo Nacional de Investigaciones Científicas y Técnicas (CONICET), Argentina. His current research interests include power electronics, electric vehicles, and renewable energy conversion.